nature COMMUNICATIONS

ARTICLE

Received 9 Nov 2016 | Accepted 11 Jan 2017 | Published 27 Feb 2017

DOI: 10.1038/ncomms14555 OPEN

Synergy of ammonium chloride and moisture on perovskite crystallization for efficient printable mesoscopic solar cells

Yaoguang Rong[1,*], Xiaomeng Hou[1,*], Yue Hu[1], Anyi Mei[1], Linfeng Liu[1], Ping Wang[1] & Hongwei Han[1]

Organometal lead halide perovskites have been widely used as the light harvester for high-performance solar cells. However, typical perovskites of methylammonium lead halides ($CH_3NH_3PbX_3$, X = Cl, Br, I) are usually sensitive to moisture in ambient air, and thus require an inert atmosphere to process. Here we demonstrate a moisture-induced transformation of perovskite crystals in a triple-layer scaffold of TiO_2/ZrO_2/Carbon to fabricate printable mesoscopic solar cells. An additive of ammonium chloride (NH_4Cl) is employed to assist the crystallization of perovskite, wherein the formation and transition of intermediate $CH_3NH_3X \cdot NH_4PbX_3(H_2O)_2$ (X = I or Cl) enables high-quality perovskite $CH_3NH_3PbI_3$ crystals with preferential growth orientation. Correspondingly, the intrinsic perovskite devices based on $CH_3NH_3PbI_3$ achieve an efficiency of 15.6% and a lifetime of over 130 days in ambient condition with 30% relative humidity. This ambient-processed printable perovskite solar cell provides a promising prospect for mass production, and will promote the development of perovskite-based photovoltaics.

[1] Michael Grätzel Center for Mesoscopic Solar Cells, Wuhan National Laboratory for Optoelectronics, School of Optical and Electronic Information, Huazhong University of Science and Technology, Wuhan 430074, China. * These authors contributed equally to this work. Correspondence and requests for materials should be addressed to H.H. (email: hongwei.han@mail.hust.edu.cn).

Organometal trihalide perovskites of methylammonium lead halides ($CH_3NH_3PbX_3$, X = Cl, Br, I) have attracted intensive research attention in the field of energy conversion due to their distinct optical and electronic properties, such as high absorption coefficient, high charge carrier mobility, long diffusion length and low defect density[1–3]. The power conversion efficiency (PCE) of perovskite solar cells (PSCs) has increased from 3.81% in 2009 (ref. 4) to a certified 22.1% in 2016, making it the fastest-advancing photovoltaic technology to date[5–8]. Besides the high efficiency, PSCs demonstrate dominant cost advantages compared with conventional silicon-based solar cells, because of low-cost raw materials and simple solution-manufacturing process. However, the degradation issue of typical perovskite $CH_3NH_3PbI_3$ associated with moisture challenges the mass production and further applications of this new-born technology[9–11].

Recently, abundant work both experimental and theoretical has been devoted to investigating the degradation of $CH_3NH_3PbI_3$ associated with moisture and develop ambient stable devices. Kamat *et al.* reported that hydrated perovskite phases of $CH_3NH_3PbI_3 \cdot H_2O$ and $(CH_3NH_3)_4PbI_6 \cdot 2H_2O$ will form during the initial degradation process of $CH_3NH_3PbI_3$ due to humidity[12]. While the monohydrate phase can be fully reversed by exposing the hydrated perovskite to a dry environment, the irreversible decomposition of the dihydrate phase will lead to the complete degradation of $CH_3NH_3PbI_3$ (ref. 13). Various approaches have been developed to improve the stability of PSCs against moisture, such as perovskite composition optimization[14,15], interface modification[16,17] and device encapsulation. Compared with typical three-dimensional perovskites, two-dimensional layered perovskites have exhibited greatly improved stability against humidity[18]. However, the device performance still cannot compete with that of conventional perovskite-based devices[19]. To attain stability together with high performance, Huang and co-workers[20] retained $CH_3NH_3PbI_3$ as the light absorber but bonded crosslinkable silane molecules with hydrophobic functional groups on fullerene to make the fullerene-based electron transport layer and the whole device highly water-resistant. Snaith and co-workers[21] and Menna and co-workers[22] replaced the most widely used hole transport layer of 2,2′,7,7′-tetrakis(*N*,*N*-di-p-methoxy-phenylamine)-9,9′-spirobifluorene (spiro-OMeTAD) with organic functionalized single-walled carbon nanotubes, and remarkably enhanced the device water resistance. Bella *et al.*[23] developed a multifunctional fluorinated photopolymer-coating technique, boosting the device efficiency to nearly 19% and device lifetime to over 6 months.

In achieving high-performance PSCs, the perovskite film quality such as morphology, crystallinity and defect density of the perovskite grains play a significant role. Various deposition methods such as antisolvent treatment[24], sequential two-step method[25] and vapour-assisted process[26] and so on have been developed to attain uniform and homogeneous perovskite thin films for mesoscopic or planar heterojunction PSCs. However, to depress the moisture-assisted degradation of perovskite $CH_3NH_3PbI_3$ during thin-film-formation process, these techniques usually require inert atmosphere or high vacuum conditions to restrain the environmental humidity, which usually couples with intensive energy-consumption issues and accordingly is incompatible with industrial production. The additive-assisted one-step solution-processing method is considered to meet the requirements for facile film-formation method as well as improved device stability[16,27,28]. Particularly, optimizing these methods under ambient conditions and correlating them with device performance will lead to a critical understanding of perovskite crystallization kinetics in ambient air, and provide a simple and effective way to fabricate efficient PSCs with improved moisture tolerance. Successful transfer from artwork in the glove box to application modules in ambient air will be an important milestone in the development of such low-cost photovoltaic technology.

Here we employ an additive of ammonium chloride (NH_4Cl) to tune the crystallization of perovskite $CH_3NH_3PbI_3$ in ambient air. It has been reported that NH_4Cl is able to retard the crystallization of $CH_3NH_3PbI_3$ and act as a binder to interconnect separated $CH_3NH_3PbI_3$ crystals[27,29]. However, the kinetics behind this process is still unknown. In our work, benefited from the microthick triple-layer scaffold[30,31], the phase transformation of perovskite crystals in the presence of ammonium and moisture is slowed down and can be monitored. We find a synergy of NH_4Cl and moisture on the crystallization of perovskite $CH_3NH_3PbI_3$. Through forming an intermediate of $CH_3NH_3X \cdot NH_4PbX_3(H_2O)_2$ (X = I or Cl), the crystallization of $CH_3NH_3PbI_3$ is first retarded. The moisture in ambient air accelerates the removal of ammonium, and thus induces the transition of intermediate to perovskite phase. On the basis of a triple-layer PSC architecture, the devices fabricated under ambient conditions show a PCE of 15.6%, and ambient air lifetime of over 130 days with performance maintaining ~96.7% of the initial value.

Results

Compositional and crystallographic characterizations. To achieve high-performance printable PSCs, it is critical to control the crystallization of perovskite absorbers in the triple-layer scaffold of mesoporous TiO_2 (m-TiO_2) electron-collecting layer, ZrO_2-insulating layer and carbon counter electrode layer. The precursor was prepared by dissolving 1.0 M PbI_2, 1.0 M CH_3NH_3I and 1.0 M NH_4Cl in N,N-Dimethylformamide (DMF), and simply dripped on the carbon layer of the scaffold. After a short-term thermal annealing of 10 min at 100 °C, the precursor was dried and homogeneously distributed in the active area of the scaffold, as shown in Fig. 1a. The active area is defined by the overlap section of the TiO_2, ZrO_2 and carbon layer as highlighted. Interestingly, the as-annealed sample was light brown, which is different from the colour of typical $CH_3NH_3PbI_3$ absorber[5,9,32], indicating that an intermediate phase rather than a pure perovskite phase may exist at this state (*vide infra*). After being exposed to ambient air with relative humidity (RH) of 45%, the colour of the sample turned dark brown. This distinct exterior variation implied a significant conversion from an intermediate to perovskite phase that occurred during the ambient exposure, leading to homogeneous distribution of $CH_3NH_3PbI_3$ absorbers in the scaffold, as shown in Fig. 1b.

According to the thermal gravimetric analysis (TGA) results of $CH_3NH_3PbI_3$/DMF, $CH_3NH_3PbI_3$/NH_4Cl and pure NH_4Cl (Fig. 1c,d), the thermal annealing process (defined as crystallization step-1) resulted in the evaporation of solvent in the precursor along with partial decomposition of NH_4Cl, since sample of $CH_3NH_3PbI_3$/DMF shows distinct weight loss between 100 and 120 °C, while the sample of $CH_3NH_3PbI_3$/NH_4Cl only shows tiny weight loss below 150 °C. Pure NH_4Cl or NH_4Cl/$CH_3NH_3PbI_3$ began to lose weight until the temperature increased to over 200 °C. During the thermal annealing process at 100 °C, NH_4Cl decomposed and released NH_3 gas, which has been confirmed by annealing the sample in a Petri dish with pH test paper (Supplementary Fig. 1). The residual NH_4Cl after thermal annealing process was detected using the Glow Discharge Optical Emission Spectrometry analysis (Supplementary Fig. 2). Thus, after crystallization step-1, an intermediate with the composition of $CH_3NH_3I \cdot PbI_2 \cdot xNH_4Cl$ ($x < 1$) may exist in the scaffold.

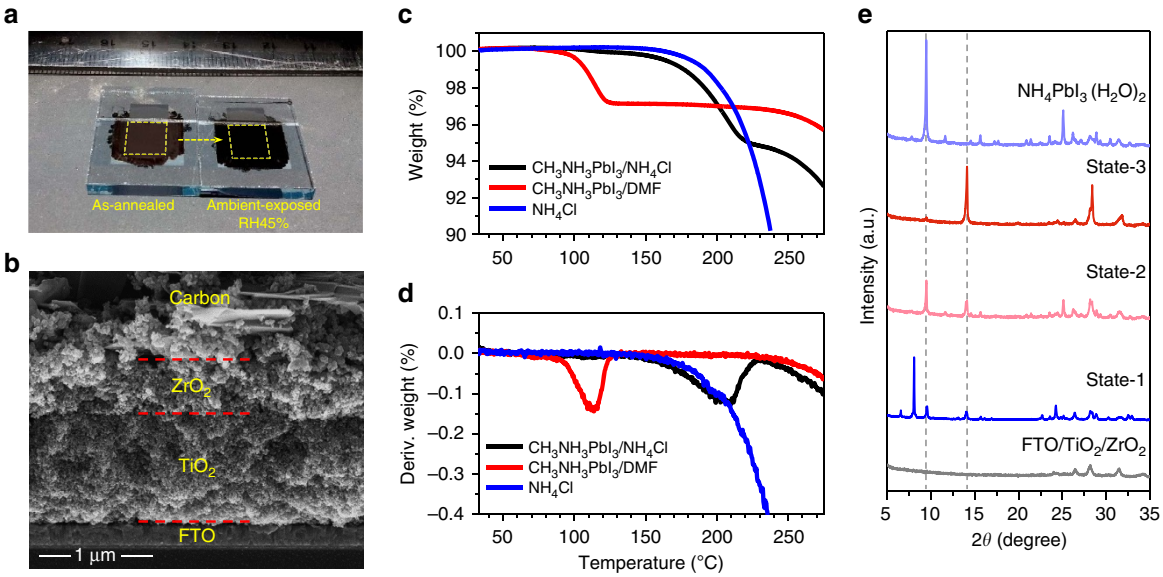

Figure 1 | Compositional and crystallographic characterization. (**a**) Digital images (from the glass side) of the as-annealed (crystallization step-1: 100 °C for 10 min) and ambient-exposed (crystallization step-2: relative humidity 45% for 36 h) precursor-infiltrated triple-layer scaffold. The active area of the device is marked with a yellow rectangle. (**b**) Cross-sectional SEM image of perovskite-infiltrated TiO_2/ZrO_2/Carbon triple layer. The triple layer was deposited by screen-printing techniques, and the perovskite absorber was deposited using an NH_4Cl-containing precursor solution and a moisture-induced crystallization process. (**c**,**d**) TGA results for the samples of $CH_3NH_3PbI_3/NH_4Cl$ (red), $CH_3NH_3PbI_3$/DMF (grey) and pure NH_4Cl (blue). (**e**) X-ray diffraction patterns of the scaffold ($FTO/TiO_2/ZrO_2$), precursor-infiltrated scaffold in state-1 (as-infiltrated), state-2 (solvent-evaporated) and state-3 (annealed), and $NH_4PbI_3(H_2O)_2$-infiltrated scaffold.

The structural information of the intermediate and phase transition was collected using X-ray diffraction measurements as shown in Fig. 1e. To avoid the interference caused by carbon layer, the precursor was infiltrated in the scaffold of m-TiO_2/ZrO_2. The as-infiltrated sample (state-1) showed distinct solvent-associated peaks between $2\theta = 5°$ and 10° (ref. 33). After exposure to ambient air at RT for several minutes, the solvent of DMF in the precursor evaporated (state-2) and the peaks at 9.46° and 14.10° significantly enhanced, which can be assigned to (101) of $NH_4PbI_3(H_2O)_2$ and (110) of $CH_3NH_3PbI_3$ crystal[34,35]. It was proposed that NH_4^+ can form perovskite NH_4PbI_3 with a calculated bandgap of 1.53 eV (ref. 36). However, since the calculated Goldschmidt tolerance factor of this compound lies close to the stability limit, it may exist in quasi-one-dimensional structures (Supplementary Fig. 3) especially in the presence of moisture[34,37]. For the thermal annealed sample (state-3), the peak at 9.46° largely reduced while the peak at 14.10° significantly enhanced, indicating that a significant transformation from $NH_4PbI_3(H_2O)_2$ to $CH_3NH_3PbI_3$ occurred during the thermal annealing process, in which a large amount of NH_3 was released. Through identifying the composition and structure of the intermediate, it can be concluded that, in the presence of NH_4^+ and moisture, the $[PbI_6]^{4-}$ octahedral will first form $[PbI_3]^-$ double chains and then bond together by NH_4^+ and water molecules, which retards the formation of $CH_3NH_3PbI_3$. The intermediate is considered a mixture of $CH_3NH_3X \cdot NH_4PbX_3(H_2O)_2$ (X = I or Cl). As the amount of ammonium reduced during thermal annealing, CH_3NH_3X will immediately combine with PbX_2 and form perovskite $CH_3NH_3PbX_3$.

Device performance under ambient conditions. To gently convert the intermediate to perovskite $CH_3NH_3PbI_3$ in the triple-layer scaffold, ambient exposure process (defined as crystallization step-2) was carried out under ambient conditions with RH of 35–65%. According to the Grotthuss mechanism[38], the water molecule is able to remove one proton from ammonium. The deprotonation of ammonium in $CH_3NH_3X \cdot NH_4PbX_3(H_2O)_2$ leads to the formation of NH_3, and HI or HCl. Since ammonia is extremely volatile and soluble in water, this moisture-induced reaction will continue until ammonium in the intermediate completely decomposes. Significantly, a reversible intercalation of NH_3 in the perovskite crystal lattice was also observed in such triple-layer scaffold-hosted $CH_3NH_3PbI_3$ (Supplementary Movie 1). Thus, once NH_4^+ in the intermediate turns to NH_3, it will release, not trap in the scaffold, facilitating the crystallization of $CH_3NH_3PbI_3$.

Figure 2a presents the evolution of device performance during this process. Surprisingly, the intermediate $CH_3NH_3X \cdot NH_4PbX_3(H_2O)_2$ containing devices still showed initial efficiencies of 8–9%, indicating that NH_4^+ did not completely restrain but only partially inhibit the crystallization of perovskite. Generally, when the as-annealed devices were exposed to ambient air, the efficiencies increased dramatically in the first 10–48 h, and then remained stable (RH35%), decreased slightly (RH45% and RH55%), or decayed sharply (RH65%). This remarkable enhancement in device performance indicated the formation of high-quality perovskite absorber in the triple-layer scaffold under ambient conditions, since the evolution occurred with the colour change of the device (from glass side) from light brown to dark brown (Fig. 2b). On the contrary, for the device stored in N_2, no distinguishable colour change can be observed, indicating that such transition needs to be induced by ambient air. It has been confirmed that the ambient condition can accelerate the decomposition of NH_4Cl (Supplementary Fig. 4). Considering that the higher RH values caused faster efficiency enhancement, it can be concluded that the moisture in ambient air plays a critical role for the crystallization of $CH_3NH_3PbI_3$, and controlling the RH for device fabrication might lead to high-performance devices. At the same time, the degradation occurred over

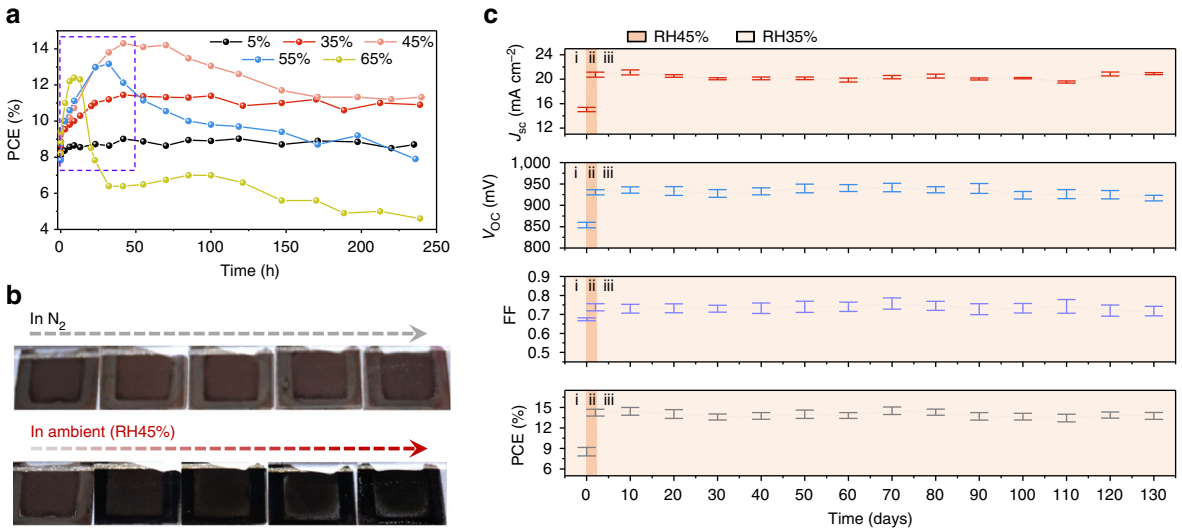

Figure 2 | Comparison of the device performance under ambient conditions. (**a**) PCE variations of as-annealed devices stored under ambient conditions with RH5–65%. The significant improvement in efficiency is marked with a purple rectangle. (**b**) Digital images (from the glass side) of the as-annealed devices stored in inert (N_2) and ambient atmosphere (RH45%). (**c**) Variations of J_{SC}, V_{OC}, FF and PCE of devices upon fabricating and ageing under ambient condition without encapsulation ((i) device fabrication except the ambient exposure, RH35%; (ii) ambient exposure, RH45%; (iii) long-term storage, RH35%). Error bars represent s.d. calculated from four devices prepared at the same conditions.

RH45% after reaching peak efficiencies should be effectively prevented.

Considering that the ambient condition of RH45% that led to the highest efficiency and that devices at RH35% presented almost no degradation, devices were fabricated at RH35% (i), exposed to RH45% (ii) and stored at RH35% (iii), as shown in Fig. 2c. After reaching an efficiency of ~14%, the devices were stored in the dark at room temperature (RT, 25 °C) without encapsulations. In a period of 130 days, all the four photovoltaic parameters of short-circuit current density (J_{SC}), open-circuit voltage (V_{OC}), fill factor (FF) and PCE stayed constant. Particularly, the PCE maintained 96.7% of the initial value after over 130-day storage. These results demonstrate that the penetration of moisture into the perovskites is effectively prevented or inhibited. In the case of RH < 35%, moisture in the ambient air will not combine with the perovskite absorbers in the scaffold and cause degradation. This agrees with the result obtained by the as-annealed device stored in RH35%. At a low RH, the moisture neither penetrates into the intermediate in the scaffold nor accomplishes the crystallization of perovskite $CH_3NH_3PbI_3$. Thus, the efficiency of the device only slightly increased to ~11% and stayed unchanged during the ambient exposure.

***In situ* characterizations of intermediate during ambient exposure.** In order to investigate the transformation during the ambient exposure, *in situ* characterizations of intermediate-infiltrated m-TiO_2 layer, ZrO_2 layer or TiO_2/ZrO_2/Carbon triple layer were performed. Although the moisture-induced crystallization process in the triple-layer scaffold, which is significantly influenced by the layer thickness and microstructure, could be different from that in a single layer, the results still provide an insight into the transformation of the intermediate and correlate it with device performance. The Fourier transform infrared spectroscopy (FTIR) measurements were performed with intermediate hosted by FTO/ZrO_2 scaffold. As exposed to the ambient air, the peak area between 2,890 and 3,340 cm^{-1} that corresponds to the vibration of N–H significantly decreased (Supplementary Fig. 5), indicating the reduction of NH_4^+ or $CH_3NH_3^+$ in the sample. An area of 100 μm × 100 μm on the sample was selected to perform an *in situ* FTIR mapping measurement, as shown in Fig. 3a. The intensity was calculated by the peak area (2,890–3,340 cm^{-1}). In the first 6 h, no distinct variation was observed, but after 12 h the signal intensity began to decrease. Further exposed to ambient air for 24 and 36 h, the signal for N–H vibration kept decreasing. For each single image during this process, the tiny variation indicated homogeneous distribution of $CH_3NH_3X \cdot NH_4PbX_3(H_2O)_2$ and $CH_3NH_3PbI_3$, and the moisture-induced transition occurred continuously once started. It was also found that the transition induced by moisture originated from the edges of the devices and then continuously extended to the whole active area of the device (Supplementary Fig. 6). This implied that the moisture in ambient air penetrated into the mesoporous scaffold from the boundaries, and the combination of water molecule and ammonium occurred as a chain reaction. Of course, water molecule can also remove the proton from ammonium of $CH_3NH_3PbI_3$, leading to the decomposition of the perovskite[39]. Thus, excessive exposure to high humid (RH55-65%) ambient air has led to degradation of device performance.

X-ray diffraction measurements were performed with intermediate-infiltrated triple layer to characterize the perovskite growth during the ambient exposure, and the results are presented in Fig. 3b. For the 0 h exposed sample, peaks attributed to perovskite structure $CH_3NH_3PbI_3$ are quite weak, although the (002), (110), (004) and (220) peaks of $CH_3NH_3PbI_3$ in tetragonal (*I*4/*mcm*) symmetry can be distinguished. After ambient exposure, the intensities of these peaks and their combinations of (002)/(110) and (004)/(220) both significantly increased, indicating enlarged grain size and increased crystallinity. Remarkably, the intensity of the (004)/(220) peak reached a comparable intensity to (002)/(110) peak after 36 h exposure. This indicates a crystal growth with preferential orientation along the [110] direction during the moisture-induced crystallization process. At the same time, it should be noted that the peaks of perovskite hydrates or PbI_2 have not been found[12,13], indicating that no water intrusion or perovskite decomposition occurred during the ambient exposure. We propose that there is a balance

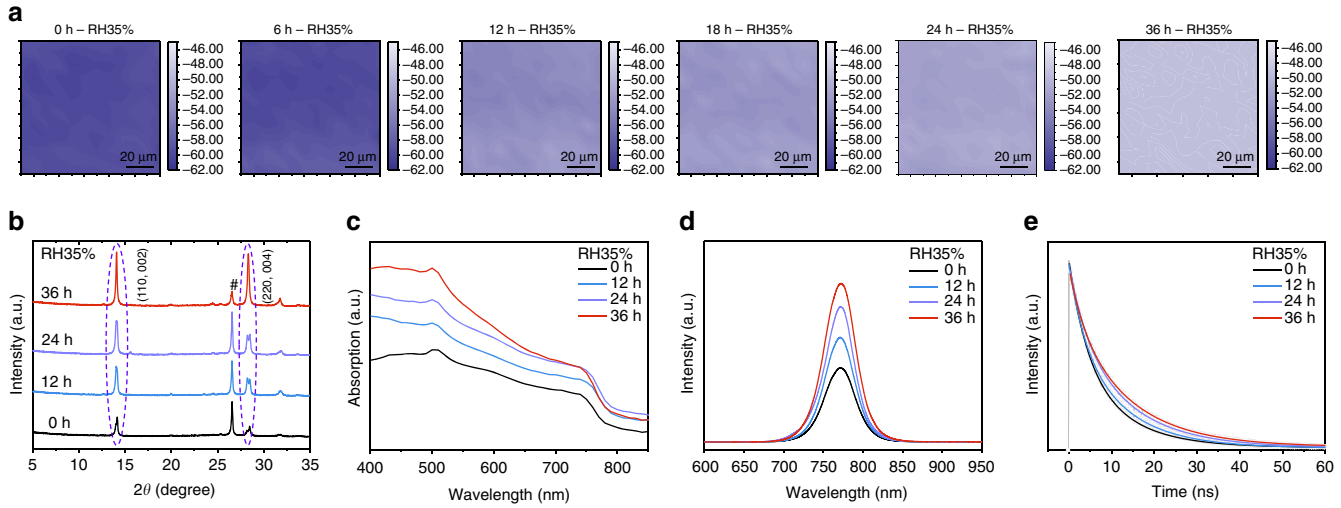

Figure 3 | *In situ* characterization of intermediate evolution in the scaffolds during ambient exposure. (**a**) *In situ* FTIR mapping measurement results of intermediate infiltrated in the ZrO_2 layer during ambient exposure (RH35%). The scanning area is 100 μm × 100 μm, and the intensity is calculated by the peak area between 2,890 and 3,340 cm^{-1}, which corresponds to the vibration of N-H. (**b**) X-ray diffraction patterns of intermediate infiltrated in TiO_2/ZrO_2/Carbon triple layer during ambient exposure (RH35% for 36 h). # represents the peak of carbon. The (110)/(002) and (220)/(004) peaks of $CH_3NH_3PbI_3$ are also marked. (**c**) Ultraviolet–visible (UV-vis) spectra of intermediate infiltrated in m-TiO_2 layer during ambient exposure (RH35% for 36 h). (**d**) Steady-state PL spectra of intermediate infiltrated in the ZrO_2 layer during ambient exposure (RH35% for 36 h). (**e**) Time-resolved PL spectra of intermediate infiltrated in the ZrO_2 layer during ambient exposure (RH35% for 36 h).

between the water in the intermediate/perovskite-infiltrated scaffold and in ambient exposure. It is much easier for NH_4PbI_3 to form hydrates compared with $CH_3NH_3PbI_3$ in ambient air. Thus, at a low RH such as 35%, the water molecules only combine with NH_4^+ in the intermediate, but will not negatively influence the perovskite crystals. Along with the phase transformation, the morphology of the perovskite absorber in the triple-layer scaffold would also slightly evolve. Since the perovskite crystal growth was significantly templated by scaffold without any capping layer, the morphology of the perovskite absorber will not change drastically during the ambient exposure process.

During the ambient exposure, the absorption of intermediate-infiltrated m-TiO_2 layer also significantly enhanced (Fig. 3c). Considering all the samples show an onset at 750 nm, which matches with the result of typical tetragonal perovskite phase of $CH_3NH_3PbI_3$, we suppose NH_4^+ only partially retard the crystallization of the perovskite absorber, since $NH_4PbX_3(H_2O)_2$ shows a colour of light yellow and no absorption in the range of 450–900 nm (Supplementary Fig. 7). *In situ* photoluminescence (PL) spectra of ZrO_2/intermediate were measured to correlate the quality of the perovskite absorber in the scaffold with the moisture-induced crystallization. Upon exposure, the peak intensity at 773 nm significantly increased, but no distinguishable peak shift can be observed in the steady-state PL spectra (Fig. 3d). For the time-resolved PL spectra, the charge carrier lifetime slightly increased from 11.50 to 13.33 ns (Fig. 3e).

Discussion

Similar results that moisture can assist the growth of perovskite films and improve the film quality, grain size and carrier lifetime have been reported[40,41]. More directly, water was added to the perovskite precursor to tune the crystallization of $CH_3NH_3PbI_{3-x}Cl_x$ (ref. 42). However, in our case, the crystallization of perovskite $CH_3NH_3PbI_3$ was determined by the synergy of NH_4Cl and moisture. We proposed a potential mechanism in view of microscopic dynamics as shown in Fig. 4. In the first stage, the solvent molecules intercalated in PbI_2 when CH_3NH_3I, PbI_2 and NH_4Cl dissolved in DMF[33,43]. As the solvent evaporated, NH_4^+ and PbX_3^- formed an ammonium lead triiodide dehydrate of $NH_4PbX_3(H_2O)_2$. After a short-term thermal annealing, $NH_4PbX_3(H_2O)_2$ released NH_3 and combined with $CH_3NH_3^+$, partially transforming to perovskite $CH_3NH_3PbI_3$. Such fast decomposition led to uncontrolled crystallization of $CH_3NH_3PbI_3$, producing a poor crystallinity of the resulting perovskite polycrystalline layer with a tiny amount of residual $NH_4PbX_3(H_2O)_2$ and CH_3NH_3I distributed in the mixed intermediate phase. Because of the presence of NH_4^+ in/between the crystals, the crystallization of $CH_3NH_3PbI_3$ was retarded. During the ambient exposure process, moisture induced the removal of NH_4^+ and facilitated the crystallization of $CH_3NH_3PbI_3$. At the final stage, the crystal growth with preferential orientation along the [110] direction was considered to be caused by chlorine in the system[44]. X-ray photoelectron spectroscopy measurements that were performed after thermal annealing and after ambient exposure confirmed that a trace amount of chlorine existed in the resulting perovskite-infiltrated triple-layer scaffold (Supplementary Fig. 8).

To fabricate high-performance devices and correlate the intermediate transformation with device performance, the RH was carefully controlled at 45% for ambient exposure and then decreased to <35% for storage. The current density–voltage (J–V) curves of the as-annealed device during 0–36 h ambient exposure is presented in Supplementary Fig. 9. It can be found that the enhancement in PCE was mainly attributed to the improved J_{SC}, which dramatically increased from 15.16 to 20.67 mA cm^{-2}. A modest increase in V_{OC} and FF negligibly contributed to the improved device performance. The enhanced photocurrent density was confirmed by incident photon-to-electron conversion efficiency (IPCE) spectra (Supplementary Fig. 10), for which the integrated current values showed an error of less than 5% compared with those measured in J–V measurements. Since the 1 μm-thick m-TiO_2 in the triple-layer device can provide sufficient contact area for the perovskite absorber, we proposed that the electron injection efficiency was a

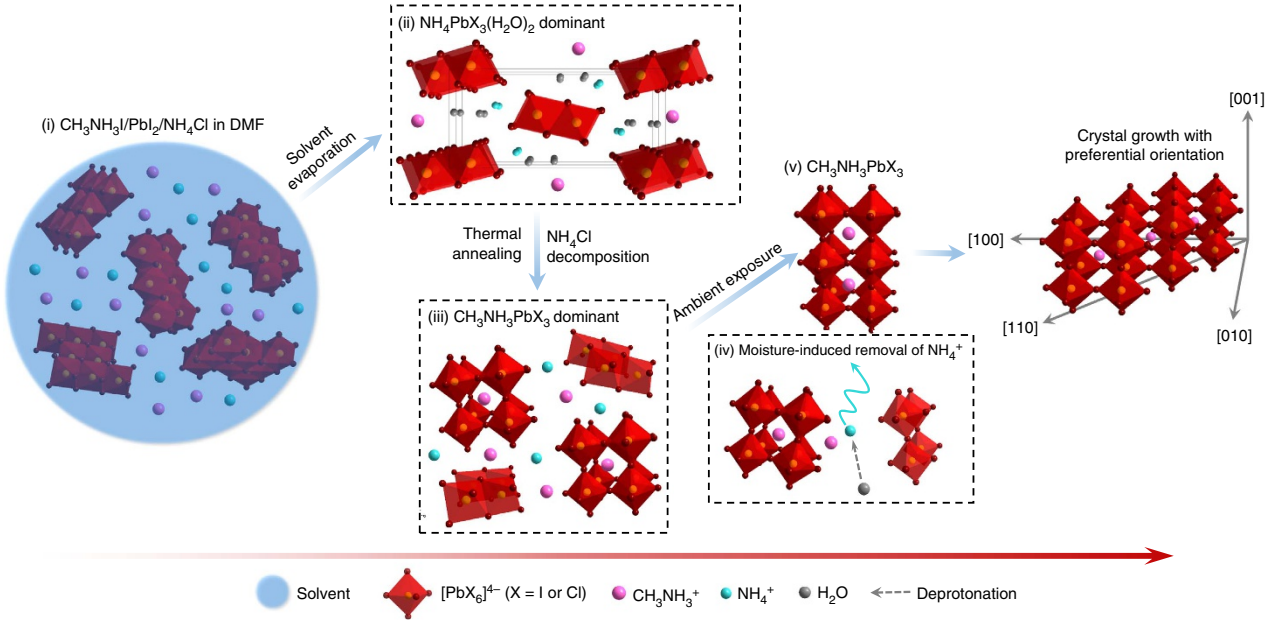

Figure 4 | Schematic view of the crystal growth process of perovskite $CH_3NH_3PbX_3$ in the presence of ammonium and moisture. (i) CH_3NH_3I, PbI_2 and NH_4Cl dissolved in DMF. (ii) As the solvent evaporated, NH_4^+ and PbX_3^- formed dominantly an ammonium lead trihalide dehydrate of $NH_4PbX_3(H_2O)_x$. (iii) During thermal annealing, $NH_4PbX_3(H_2O)_x$ released NH_3 and combined with $CH_3NH_3^+$, partially transforming to perovskite $CH_3NH_3PbX_3$. (iv) Moisture induced the removal of NH_4^+ and facilitated the (v) crystallization of $CH_3NH_3PbX_3$. At the final stage, $CH_3NH_3PbX_3$ crystals grew along the [110] direction.

constant. The transition from $CH_3NH_3X \cdot NH_4PbX_3(H_2O)_2$ to $CH_3NH_3PbI_3$ mainly contributed to the enhancement in light-harvesting efficiency and charge collection efficiency for IPCE. After 36 h exposure, the IPCE increased dramatically from 60 to over 80% in the range of 400–650 nm with peak close to 90%. These increases in IPCE and J_{SC} were in accordance with the enhanced absorption spectra as presented in Fig. 3c.

A champion efficiency of 15.60% with J_{SC} of 21.45 mA cm^{-2}, V_{OC} of 0.94 V and FF of 0.77 was achieved for such ambient-processed printable PSCs, as shown in Fig. 5a. The *J*–*V* curves were measured at a scan rate of 100 mV s^{-1}. Comparing the *J*–*V* curves measured with reverse and forward scans, a slight hysteresis phenomenon existed, mainly showing tiny variation in FF. Stabilized output measurement was performed to evaluate the accurate PCE of the device. Under a bias of 0.76 V, the current sharply increased to 20.33 mA cm^{-2} once exposed to 1 sun illumination, demonstrating an efficiency of 15.45% (Fig. 5b). This efficiency is quite close to the values obtained in the *J*–*V* measurements.

On the basis of the previous discussions, 30 devices were fabricated using the optimal two-step crystallization-involved method. The photovoltaic parameters of the device for step-1 and step-2 are compared, and the results obtained with traditional one-step method are plotted as a reference (Fig. 5c–f and Table 1). The control devices show average PCE of 6.77%, and the poor device performance is mainly due to the relatively low average J_{SC} of 14.04 mA cm^{-2} and FF of 0.55. Incomplete pore-filling of perovskite absorber limited the light-harvesting and charge transportation. For the devices fabricated in step-1, similar efficiencies were obtained though V_{OC} and FF varied. The low J_{SC} was caused by the retarded crystallization of perovskite absorbers, not the incomplete pore-filling. After ambient exposure as step-2, the device efficiency significantly improved to an average value of 13.92% along with increased average J_{SC} of 20.21 mA cm^{-2}, V_{OC} of 0.935 V and FF of 0.73. Detailed distributions of the photovoltaic parameters are presented in Supplementary Fig. 11.

In summary, we report a synergy effect of NH_4Cl and moisture on perovskite crystallization in printable PSCs. The NH_4Cl and moisture-assisted deposition method provides a facile way to accomplish complete pore-filling of perovskite absorbers in the mesoporous triple-layer scaffold, which plays a significant role in attaining efficient and stable printable PSCs. A comprehensive understanding of the mechanism that NH_4^+ retarded and a moisture-induced crystallization process is built. Correspondingly, the devices based on $CH_3NH_3PbI_3$ achieve an average PCE of 13.92% with a champion efficiency of 15.60% and a lifetime of over 130 days in ambient air with RH of 35%. This design and strategy suggest promising prospects for further mass production of perovskite-based photovoltaics and will significantly promote the development of perovskite-based photovoltaics.

Methods

Materials. Unless stated otherwise, all materials were purchased from Sigma-Aldrich or Acros Organics and used as received. CH_3NH_3I was synthesized and purified according to literature procedures[45]. The perovskite precursor solution was prepared by dissolving PbI_2 (461 mg, 1.0 M) and CH_3NH_3I (159 mg, 1.0 M) with/without NH_4Cl (53.5 mg, 1.0 M) in DMF (1.0 ml), and stirred at 70 °C for 30 min. The TiO_2, ZrO_2 and carbon pastes were prepared as previously reported[30].

Device fabrication. Unless stated otherwise, the whole device fabrication process was carried out under ambient conditions (RH35%). The FTO-coated glass substrates (Tec15, Pilkington) were first etched by laser and cleaned by ultrasonication with detergent, deionized water, acetone and ethanol. A compact TiO_2 layer was then deposited on the patterned substrates by aerosol spray pyrolysis at 450 °C using a titanium diisopropoxide bis(acetylacetonate) solution diluted in ethanol (1:39, volume ratio). After cooling to RT (25 °C), a 1 μm-thick mesoporous TiO_2 layer, a 1 μm-thick ZrO_2 spacer layer and a 10 μm-thick carbon layer were screen-printed on the substrates layer by layer. The TiO_2 and ZrO_2 layers were sintered at 450 °C for 30 min, and the carbon layer was sintered at 400 °C for 30 min, forming the mesoporous triple-layer-based scaffold. After cooling to RT, the precursor solution with or without NH_4Cl was infiltrated into the triple layer by drop-casting via the edge of the carbon layer. After annealing at 100 °C for 10 min (crystallization step-1: thermal annealing), the as-annealed samples were exposed to ambient conditions with RH of 5–65% (crystallization step-2: ambient exposure). The ambient exposure was performed in an environmental chamber

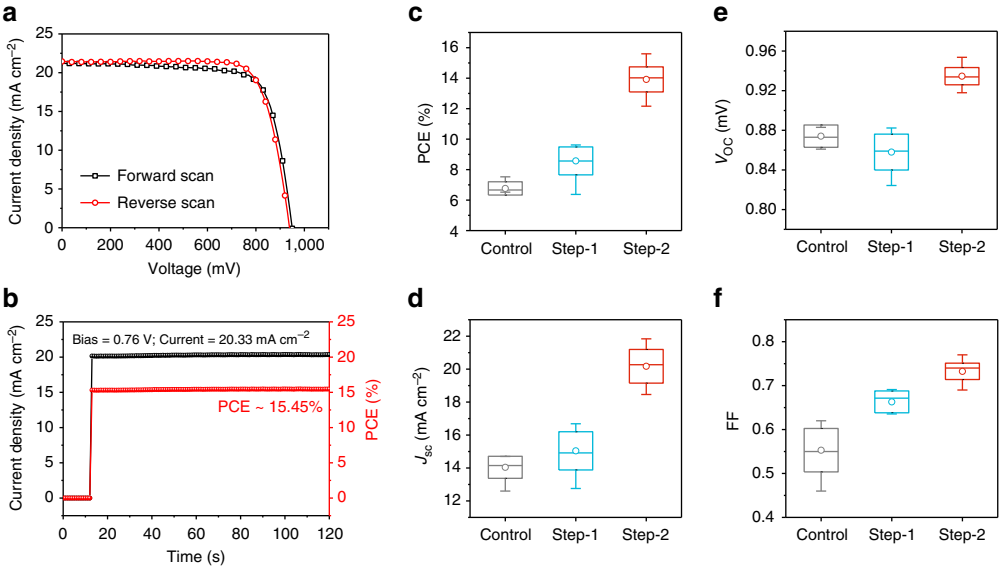

Figure 5 | Performance of the champion device and distributions of device photovoltaic parameters. (**a**) *J*–*V* curves of the champion device using NH_4Cl-containing precursor and moisture-induced crystallization process measured by reverse scan (RS) and forward scan (FS) with a scan rate of 100 mV s^{-1}. RS: V_{OC} = 0.94 V, J_{SC} = 21.45 mA cm^{-2}, FF = 0.77, PCE = 15.60%; FS: V_{OC} = 0.95 V, J_{SC} = 21.20 mA cm^{-2}, FF = 0.75, PCE = 15.17%. (**b**) Stabilized output of the device measured under a bias of 0.76 V, presenting a current density of 20.33 mA cm^{-2} and a PCE of 15.45%. (**c**–**f**) Histograms of PCE, J_{SC}, V_{OC} and FF of devices fabricated using conventional drop-casting method with precursor of PbI_2 and CH_3NH_3I in DMF (control), and moisture-induced crystallization method (step-1 for thermal annealing, step-2 for ambient exposure) with precursor of PbI_2, CH_3NH_3I and NH_4Cl in DMF. The data are represented as a standard box plot where the box range, median line and circle dot are defined by the s.d., middle value and average value. The whiskers represent the outlier values with a coefficient of 1.5. The results are summarized from 30 devices.

Table 1 | Photovoltaic parameters for printable PSCs fabricated with conventional drop-casting method (control) and moisture-induced crystallization method.

Sample method	V_{OC} (V)	J_{SC} (mA cm^{-2})	FF	PCE (%)
Control	0.874 ± 0.011	14.04 ± 0.67	0.553 ± 0.049	6.77 ± 0.44
Step-1	0.858 ± 0.018	15.04 ± 1.16	0.663 ± 0.025	8.57 ± 0.92
Step-2	0.935 ± 0.009	20.21 ± 1.03	0.733 ± 0.019	13.92 ± 0.82

FF, fill factor; PCE, power conversion efficiency; PSC, perovskite solar cell.
s.d.'s are calculated from 30 cells for each method.
Step-1 for thermal annealing, step-2 for ambient exposure.

(Vötsch, C4-180), which can provide an ambient condition with RH of 10–98% (deviation: ± 1 to ± 3%), or in a dry-air (RH ≤ 5%) filled glove box. For the fabrication of the best-performing devices exhibiting a PCE of over 15%, crystallization step-2 was performed under RH45% for 48 h, and all the other procedures were carried out under RH35%.

Characterization. The cross-sectional scanning electron microscopy (SEM) image of the perovskite-infiltrated triple layer was obtained by a field-emission scanning electron microscope (Nova NanoSEM 450, FEI). The TGA measurements were carried out at a heating rate of 10 °C min^{-1} under nitrogen or ambient airflow (Pyris1 TGA, PerkingElmer). The *in situ* characterizations of FTIR, X-ray diffraction, UV–vis and PL spectra were performed at RH35% in ambient air. To simulate the conditions in device fabrication, the samples were prepared by depositing intermediate in TiO_2 layer, ZrO_2 layer or TiO_2/ZrO_2/carbon triple layer on FTO glass substrates. The FTIR measurements (Vertex 70, Bruker) were performed with the FTO/ZrO_2/intermediate. The X-ray diffraction measurements were performed on an X-ray diffractometer (X'pert PRO, Cu Kα radiation, 40 kV) and detected through the intermediate side of FTO/TiO_2/ZrO_2/carbon/intermediate. The UV–vis spectra were obtained with FTO/TiO_2/intermediate on a spectrophotometer (LabRAM HR800, Horiba). The steady-state and time-resolved PL measurements of FTO/ZrO_2/intermediate were carried out on a fluorescence spectrometer (DeltaFlex, Horiba). Glow Discharge Optical Emission Spectrometry measurement was performed on GD-Profiler 2 (Horiba). Photocurrent density–voltage (*J*–*V*) curves were characterized with a Keithley 2400 sourcemeter and a Newport solar simulator (model 91192). The power of the simulated light was calibrated to 100 mW cm^{-2} using a Newport Oriel PV reference cell (model 91150 V). The active area of the device is ~0.8 cm^2, and a black mask with a circular aperture (0.126 cm^2) was applied for *J*–*V* measurements. The *J*–*V* testing was performed with both reverse and forward scan directions at 100 mV s^{-1} (sweep delay time of 100 ms). No preconditioning protocol was used before the characterization. The IPCE spectra were measured using a 150 W xenon lamp (Oriel) fitted with a monochromator (Cornerstone 74004) as a monochromatic light source. Calibration with the Oriel Si detector was carried out before IPCE measurements. Unless stated otherwise, all the measurements were carried out at RH35% and RT, which was controlled by the air conditioner at the testing centre.

Data availability. The data supporting the findings of this study are available from the corresponding author upon request.

References

1. Dong, Q. *et al.* Electron-hole diffusion lengths > 175 μm in solution-grown $CH_3NH_3PbI_3$ single crystals. *Science* **347,** 967–970 (2015).
2. Xing, G. *et al.* Long-range balanced electron-and hole-transport lengths in organic-inorganic $CH_3NH_3PbI_3$. *Science* **342,** 344–347 (2013).
3. Shi, D. *et al.* Low trap-state density and long carrier diffusion in organolead trihalide perovskite single crystals. *Science* **347,** 519–522 (2015).
4. Kojima, A., Teshima, K., Shirai, Y. & Miyasaka, T. Organometal halide perovskites as visible-light sensitizers for photovoltaic cells. *J. Am. Chem. Soc.* **131,** 6050–6051 (2009).
5. Green, M. A., Ho-Baillie, A. & Snaith, H. J. The emergence of perovskite solar cells. *Nat. Photon.* **8,** 506–514 (2014).
6. Li, X. *et al.* A vacuum flash–assisted solution process for high-efficiency large-area perovskite solar cells. *Science* **353,** 58–62 (2016).
7. Yang, W. S. *et al.* High-performance photovoltaic perovskite layers fabricated through intramolecular exchange. *Science* **348,** 1234–1237 (2015).
8. Polman, A., Knight, M., Garnett, E. C., Ehrler, B. & Sinke, W. C. Photovoltaic materials: Present efficiencies and future challenges. *Science* **352,** aad4424 (2016).
9. Stranks, S. D. & Snaith, H. J. Metal-halide perovskites for photovoltaic and light-emitting devices. *Nat. Nanotechnol.* **10,** 391–402 (2015).
10. Rong, Y., Liu, L., Mei, A., Li, X. & Han, H. Beyond efficiency: the challenge of stability in mesoscopic perovskite solar cells. *Adv. Energy Mater.* **5,** 1501066 (2015).

11. Park, N.-G., Grätzel, M., Miyasaka, T., Zhu, K. & Emery, K. Towards stable and commercially available perovskite solar cells. *Nat. Energy* **1,** 16152 (2016).
12. Christians, J. A., Miranda Herrera, P. A. & Kamat, P. V. Transformation of the excited state and photovoltaic efficiency of $CH_3NH_3PbI_3$ perovskite upon controlled exposure to humidified air. *J. Am. Chem. Soc.* **137,** 1530–1538 (2015).
13. Leguy, A. M. A. *et al.* Reversible hydration of $CH_3NH_3PbI_3$ in films, single crystals, and solar cells. *Chem. Mater.* **27,** 3397–3407 (2015).
14. Noh, J. H., Im, S. H., Heo, J. H., Mandal, T. N. & Seok, S. I. Chemical management for colorful, efficient, and stable inorganic–organic hybrid nanostructured solar cells. *Nano Lett.* **13,** 1764–1769 (2013).
15. Tai, Q. *et al.* Efficient and stable perovskite solar cells prepared in ambient air irrespective of the humidity. *Nat. Commun.* **7,** 11105 (2016).
16. Li, X. *et al.* Improved performance and stability of perovskite solar cells by crystal cross-linking with aminoalkylphosphonates. *Nat. Chem.* **7,** 703–711 (2015).
17. You, J. *et al.* Improved air stability of perovskite solar cells via solution-processed metal oxide transport layers. *Nat. Nanotechnol.* **11,** 75–81 (2016).
18. Smith, I. C., Hoke, E. T., Solis-Ibarra, D., McGehee, M. D. & Karunadasa, H. I. A layered hybrid perovskite solar-cell absorber with enhanced moisture stability. *Angew. Chem. Int. Ed.* **53,** 11232–11235 (2014).
19. Tsai, H. *et al.* High-efficiency two-dimensional Ruddlesden–Popper perovskite solar cells. *Nature* **536,** 312–316 (2016).
20. Bai, Y. *et al.* Enhancing stability and efficiency of perovskite solar cells with crosslinkable silane-functionalized and doped fullerene. *Nat. Commun.* **7,** 12806 (2016).
21. Habisreutinger, S. N. *et al.* Carbon nanotube/polymer composites as a highly stable hole collection layer in perovskite solar cells. *Nano Lett.* **14,** 5561–5568 (2014).
22. Gatti, T. *et al.* Boosting perovskite solar cells performance and stability through doping a poly-3(hexylthiophene) hole transporting material with organic functionalized carbon nanostructures. *Adv. Funct. Mater.* **26,** 7443–7453 (2016).
23. Bella, F. *et al.* Improving efficiency and stability of perovskite solar cells with photocurable fluoropolymers. *Science* **354,** 203–206 (2016).
24. Jeon, N. J. *et al.* Solvent engineering for high-performance inorganic–organic hybrid perovskite solar cells. *Nat. Mater.* **13,** 897–903 (2014).
25. Burschka, J. *et al.* Sequential deposition as a route to high-performance perovskite-sensitized solar cells. *Nature* **499,** 316–319 (2013).
26. Liu, M., Johnston, M. B. & Snaith, H. J. Efficient planar heterojunction perovskite solar cells by vapour deposition. *Nature* **501,** 395–398 (2013).
27. Chen, Y., Zhao, Y. & Liang, Z. Non-thermal annealing fabrication of efficient planar perovskite solar cells with inclusion of NH_4Cl. *Chem. Mater.* **27,** 1448–1451 (2015).
28. Zhao, Y. *et al.* A polymer scaffold for self-healing perovskite solar cells. *Nat. Commun.* **7,** 10228 (2016).
29. Zuo, C. & Ding, L. An 80.11% FF record achieved for perovskite solar cells by using the NH_4Cl additive. *Nanoscale* **6,** 9935–9938 (2014).
30. Ku, Z., Rong, Y., Xu, M., Liu, T. & Han, H. Full printable processed mesoscopic $CH_3NH_3PbI_3/TiO_2$ heterojunction solar cells with carbon counter electrode. *Sci. Rep.* **3,** 3132 (2013).
31. Mei, A. *et al.* A hole-conductor–free, fully printable mesoscopic perovskite solar cell with high stability. *Science* **345,** 295–298 (2014).
32. Zhao, Y. & Zhu, K. Organic-inorganic hybrid lead halide perovskites for optoelectronic and electronic applications. *Chem. Soc. Rev.* **45,** 655–689 (2016).
33. Hao, F., Stoumpos, C. C., Liu, Z., Chang, R. P. H. & Kanatzidis, M. G. Controllable perovskite crystallization at a gas–solid interface for hole conductor-free solar cells with steady power conversion efficiency over 10%. *J. Am. Chem. Soc.* **136,** 16411–16419 (2014).
34. Bedlivy, D. & Mereiter, K. The structures of potassium lead triiodide dihydrate and ammonium lead triiodide dihydrate. *Acta Cryst. B* **36,** 782–785 (1980).
35. Kim, H.-S. *et al.* Lead iodide perovskite sensitized all-solid-state submicron thin film mesoscopic solar cell with efficiency exceeding 9%. *Sci. Rep.* **2,** 591 (2012).
36. Filip, M. R., Eperon, G. E., Snaith, H. J. & Giustino, F. Steric engineering of metal-halide perovskites with tunable optical band gaps. *Nat. Commun.* **5,** 5757 (2014).
37. Fan, L.-Q. & Wu, J.-H. NH_4PbI_3. *Acta Cryst. E* **63,** i189–i189 (2007).
38. Agmon, N. The Grotthuss mechanism. *Chem. Phys. Lett.* **244,** 456–462 (1995).
39. Frost, J. M. *et al.* Atomistic origins of high-performance in hybrid halide perovskite solar cells. *Nano Lett.* **14,** 2584–2590 (2014).
40. Zhou, H. *et al.* Interface engineering of highly efficient perovskite solar cells. *Science* **345,** 542–546 (2014).
41. You, J. *et al.* Moisture assisted perovskite film growth for high performance solar cells. *Appl. Phys. Lett.* **105,** 183902 (2014).
42. Gong, X. *et al.* Controllable perovskite crystallization by water additive for high-performance solar cells. *Adv. Funct. Mater.* **25,** 6671–6678 (2015).
43. Rong, Y. *et al.* Solvent engineering towards controlled grain growth in perovskite planar heterojunction solar cells. *Nanoscale* **7,** 10595–10599 (2015).
44. Dong, Q. *et al.* Abnormal crystal growth in $CH_3NH_3PbI_{3-x}Cl_x$ using a multi-cycle solution coating process. *Energy. Environ. Sci.* **8,** 2464–2470 (2015).
45. Etgar, L. *et al.* Mesoscopic $CH_3NH_3PbI_3/TiO_2$ heterojunction solar cells. *J. Am. Chem. Soc.* **134,** 17396–17399 (2012).

Acknowledgements

We acknowledge financial support from the National Natural Science Foundation of China (91433203, 61474049), the Ministry of Science and Technology of China (2015AA034601), the 111 Project (No. B07038) and the Science and Technology Department of Hubei Province (2013BAA090). We also thank the Analytical and Testing Center of Huazhong University of Science and Technology for FESEM testing.

Author contributions

H.H. and Y.R. designed and directed this study, analysed results and co-wrote the manuscript. Y.R., X.H. and Y.H. conducted most of the device fabrication and measurements. A.M. conducted the SEM measurements. L.L. performed the X-ray diffraction measurements. P.W. assisted on the characterizations of FTIR. All the authors contributed to the discussion of the manuscript.

Additional information

Supplementary Information accompanies this paper at http://www.nature.com/naturecommunications

Competing financial interests: The authors declare no competing financial interests.

Reprints and permission information is available online at http://npg.nature.com/reprintsandpermissions/

How to cite this article: Rong, Y. *et al.* Synergy of ammonium chloride and moisture on perovskite crystallization for efficient printable mesoscopic solar cells. *Nat. Commun.* **8,** 14555 doi: 10.1038/ncomms14555 (2017).

Publisher's note: Springer Nature remains neutral with regard to jurisdictional claims in published maps and institutional affiliations.